

Supplementary Materials

1. The Original Names of the Images from BigNeuron Dataset

TABLE S1 THE ORIGINAL NAMES OF THE BIGNEURON IMAGES USED IN THIS WORK

Image ID	Original Name
BigNeuron 1	p_checked7_janelia_flylight_part1\GMR_57C10_AD_01-Two_recombinase_flipouts_A-f-A-20111107_2_C5-right_optic_lobe.v3draw.extract_0
BigNeuron 2	p_checked7_janelia_flylight_part1\GMR_57C10_AD_01-Two_recombinase_flipouts_A-f-A-20111108_2_F3-right_optic_lobe.v3draw.extract_0_30
BigNeuron 3	p_checked7_janelia_flylight_part1\GMR_57C10_AD_01-Two_recombinase_flipouts_A-m-A-20111006_1_A4-right_optic_lobe.v3draw.extract_0
BigNeuron 4	p_checked7_janelia_flylight_part1\GMR_57C10_AD_01-Two_recombinase_flipouts_A-m-A-20111006_1_E1-right_optic_lobe.v3draw.extract_4
BigNeuron 5	p_checked6_human_culturedcell_Cambridge_in_vitro_confocal_GFP\Image4
BigNeuron 6	p_checked6_human_culturedcell_Cambridge_in_vitro_confocal_GFP\Image7
BigNeuron 7	p_checked6_human_culturedcell_Cambridge_in_vitro_confocal_GFP\Image10
BigNeuron 8	p_checked6_human_culturedcell_Cambridge_in_vitro_confocal_GFP\Image31
BigNeuron 9	p_checked6_fruitfly_larvae_gmu\done_1_CL-I_X_OREGON_R_ddaD_membrane-GFP
BigNeuron 10	p_checked6_fruitfly_larvae_gmu\done_1_CL-I_X_OREGON_R_ddaE_membrane-GFP
BigNeuron 11	p_checked6_fruitfly_larvae_gmu\done_2_CL-I_Membrane-GFP_X_F-Actin-Red_ddaD_Membrane-GFP_F-Actin-Red.czi_C_1
BigNeuron 12	p_checked6_fruitfly_larvae_gmu\done_Result_of_C1-CL-I(X-Mas)_x_OregonR_ddaE_F-actinGFP_MT-Red
BigNeuron 13	p_checked6_fruitfly_larvae_gmu\done_2_CL-I_Membrane-GFP_X_F-Actin-Red_ddaE_Membrane-GFP_F-Actin-Red.czi_C_1
BigNeuron 14	p_checked6_fruitfly_larvae_gmu\done_3_CL-I_MT_X_MYR-GFP_ddaD_MT-mCherry_membrane-GFP.czi_C_1
BigNeuron 15	p_checked6_fruitfly_larvae_gmu\done_err_3_CL-I_MT_X_MYR-GFP_ddaE_MT-mCherry_membrane-GFP.czi_C_1
BigNeuron 16	p_checked6_mouse_RGC_uw\ho_091201c1
BigNeuron 17	p_checked6_mouse_RGC_uw\ho_091202c2
BigNeuron 18	p_checked6_mouse_RGC_uw\ho_091204c2
BigNeuron 19	p_checked6_mouse_RGC_uw\ho_140921c3
BigNeuron 20	p_checked6_mouse_RGC_uw\ho_140921c5
BigNeuron 21	p_checked6_mouse_RGC_uw\ho_140921c9
BigNeuron 22	p_checked6_mouse_RGC_uw\HO_140921c14
BigNeuron 23	p_checked6_mouse_RGC_uw\HO_140921c22
BigNeuron 24	p_checked6_mouse_RGC_uw\sv_080926a
BigNeuron 25	p_checked6_mouse_RGC_uw\sv_091226c2
BigNeuron 26	p_checked6_mouse_RGC_uw\sv_100110c4
BigNeuron 27	p_checked6_mouse_RGC_uw\SV_140918c7

BigNeuron 28	p_checked6_mouse_RGC_uw\sv_140918c8
BigNeuron 29	p_checked6_mouse_RGC_uw\sv_140921c1
BigNeuron 30	p_checked6_mouse_RGC_uw\sv_140921c4
BigNeuron 31	p_checked6_mouse_RGC_uw\sv_140921c6
BigNeuron 32	p_checked6_mouse_RGC_uw\sv_140921c12
BigNeuron 33	p_checked6_mouse_RGC_uw\SV_140921c16
BigNeuron 34	p_checked6_mouse_RGC_uw\SVHO_err_140918c3

2. Hyper-Parameter Selection

The scale factor λ controls the size of the local region Θ for seed point searching in the joint decision scheme. To assess the sensitivity of λ , we tuned it from 1 to 4 and calculate the average F1-measure of our method on the 3 test datasets (Fig. S1). It can be seen that the optimal results of our method appear when $\lambda=3$ or 4. The average F1-measure of our method on the WMBS dataset increases along with λ grows. The same trend can be observed in the NCL1A dataset. When λ is in the range of $[2,4]$, our method has relatively stable performances on all the 3 test datasets. Therefore, the default value of λ can be 3 for the BigNeuron dataset and 4 for the other two datasets. In the experiments for λ , we set $K=1024$, $N=9$, $M_a = M_p = 64$.

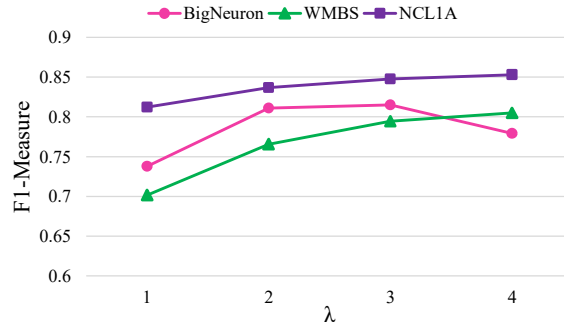


Fig. S1. The average F1-measure for different λ .

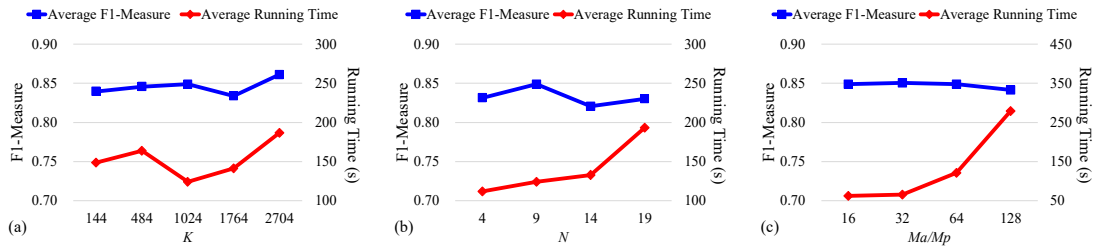


Fig. S2. (a), (b) and (c) are the line chart of the average F1-measure and running time for different K , N and Ma/Mp , respectively.

To obtain the default values for the number of predicted directions (K), the number of spherical surfaces (N), azimuth angles (M_a) and polar angles (M_p), we conducted experiments on the 34 BigNeuron test images used in this paper, and the average F1-measure and running time were used as evaluation metrics. Similar to [S1], we tuned one hyper-parameter each time and fixed the others to optimize that hyper-parameter. λ was selected between $[1,4]$ in the following experiments.

The number of predicted directions (K): To demonstrate the impact of K to our method, we set 6 values for it, i.e., $\{144, 484, 1024, 1764, 2704\}$, which are the squared values for $\{12, 22, 32, 42, 52\}$.

We set $N=9$ to ensure that sufficient local information can be extracted, and we set $M_a = M_p = 64$ according to the suggestion of a previous work [S2]. It can be seen from Fig. S2(a) that the performance of our method is stable when the value of K changes. Although $K=2704$ leads to the best performance, its running time is the longest. We selected $K=1024$ as the default value, because its average F1-measure is only 1.2% lower than that of $K=2704$, but the average running time is the shortest.

The number of spherical surfaces (N): To optimize N , we set 4 values for it, i.e., $\{4, 9, 14, 19\}$, and the radii ranges were $[2,5]$, $[2,10]$, $[2,15]$ and $[2,20]$, respectively. We fixed $K=1024$ and $M_a = M_p = 64$. It can be observed from Fig. S2(b) that $N=9$ is the optimal value, because of its acceptable running time and best performance. The performance drops when $N>9$, because of the complicated and rich hierarchy of neuronal structures in the images. Although the sphere surfaces with larger radius can extract more intensity distribution features, they also receive more noisy information from the surrounding neuronal branches, leading to worse determination results. Thus, we selected $N=9$ as the default value.

Azimuth angles (M_a) and polar angles (M_p): In the experiments, we set $M_a = M_p$ to ensure that the extracted spherical patches are squares. Therefore, M_a and M_p were optimized jointly. To optimize M_a and M_p , we set 4 values for them, i.e., $\{16, 32, 64, 128\}$, and we fixed $K=1024$ and $N=9$. Unlike the other hyper-parameters, different values for M_a and M_p result in different input image size to the proposed SPE-DNR. Thus, the network architecture of the SPE-DNR was changed slightly according to different M_a and M_p , by simply adding or removing a max pooling layer and changing the stride of the convolutional layers in the backbone of the SPE-DNR. From Fig. S2(c), we can see that the performance of our method remains stable, whereas the running time raise substantially when the value of M_a and M_p increases. The performance of our method with $M_a = M_p = 32$ is close to that with $M_a = M_p = 64$, and the running time is much shorter. Thus, the default value for M_a and M_p is 32.

3. Parameters and Operations for the Synthetic Images

The detailed parameters and operations for image synthesis are listed in Table S2, where the reconstruction names are the manual reconstruction annotations used to generated these images. The original names for the reconstruction annotations from the BigNeuron dataset are,

- Fly light 1: p_checked7_janelia_flylight_part1/GMR_57C10_AD_01-1xLwt_attp40_4stop1-m-A02-20111101_1_D3-left_optic_lobe.v3draw.extract_11
- Fly light 2: p_checked7_janelia_flylight_part1/GMR_57C10_AD_01-1xLwt_attp40_4stop1-m-A02-20111101_2_C1-left_optic_lobe.v3draw.extract_2
- Fly light 3: p_checked7_janelia_flylight_part1/GMR_57C10_AD_01-1xLwt_attp40_4stop1-m-A02-20111101_2_E4-right_optic_lobe.v3draw.extract_2
- Mouse 1: p_checked6_mouse_RGC_uw/ho_110203c3
- Mouse 2: p_checked6_mouse_RGC_uw/ho_100108c3
- Mouse 3: p_checked6_mouse_RGC_uw/ho_140918c9
- Fruit fly 1: p_checked6_fruitfly_larvae_gmu/done_Result_of_C1-CL-I(X-Mas)_x_OregonR_ddaD_F-actinGFP_MT-Red

The remaining reconstruction annotations WMBS 1 and 2 are from the WMBS dataset.

Since abrupt radius changes are not frequently observed and mainly appear in the BigNeuron images of mouse and fruitfly species, we only conducted Operation 2 on two synthetic images.

Table S2							
Image ID	Reconstruction Names	Parameters			Operations		
		BG	SNR	COR	1	2	3
1	Fly light 1	10	5	0.5	✓		
2	Fly light 1	10	10	0.5	✓		
3	Fly light 1	10	10	0.5	✓		✓
4	Fly light 1	10	20	0.5	✓		
5	Fly light 2	10	5	0.5	✓		
6	Fly light 2	10	10	0.5	✓		
7	Fly light 2	10	10	0.5	✓		✓
8	Fly light 2	10	20	0.5	✓		
9	Fly light 3	10	5	0.5	✓		
10	Fly light 3	10	10	0.5	✓		
11	Fly light 3	10	10	0.5	✓		✓
12	Fly light 3	10	20	0.5	✓		
13	Mouse 1	0	10	0.5	✓		
14	Mouse 1	0	100	2.0	✓		
15	Mouse 1	1	10	0.5	✓		✓
16	Mouse 1	10	5	0.5	✓		
17	Mouse 1	10	5	0.5	✓		✓
18	Mouse 1	10	5	0.0	✓		✓
19	Mouse 1	10	10	0.5	✓		
20	Mouse 1	10	10	1.0	✓		✓
21	Mouse 2	0	10	0.5	✓		
22	Mouse 2	0	100	2.0	✓		
23	Mouse 2	1	10	0.5	✓		✓
24	Mouse 2	10	5	0.5	✓		
25	Mouse 2	10	5	0.5	✓		✓
26	Mouse 2	10	5	0.0	✓		✓
27	Mouse 2	10	10	0.5	✓		
28	Mouse 2	10	10	1.0	✓		✓
29	Mouse 3	10	5	0.5	✓		
30	Mouse 3	10	5	0.5	✓		✓
31	Mouse 3	10	5	0.0	✓		✓
32	Mouse 3	10	10	0.5	✓		
33	Mouse 3	10	10	1.0	✓		✓
34	Mouse 3	0	10	0.5	✓		
35	Mouse 3	0	100	2.0	✓		
36	Mouse 3	1	10	0.5	✓		✓
37	Mouse 3	1	10	0.5	✓	✓	✓
38	Fruit fly 1	10	5	0.5	✓		
39	Fruit fly 1	10	5	0.5	✓		✓
40	Fruit fly 1	10	10	0.5	✓		
41	Fruit fly 1	0	10	0.5	✓		
42	Fruit fly 1	0	100	2.0	✓		
43	Fruit fly 1	1	10	0.5	✓		✓
44	Fruit fly 1	1	10	0.5	✓	✓	✓
45	WMBS 1	5	5	0.5	✓		
46	WMBS 1	5	5	0.7	✓		
47	WMBS 2	5	5	0.5	✓		
48	WMBS 2	5	5	0.7	✓		

4. Evaluation Results of the SPE-DNR Trained on Real Images

We trained the SPE-DNR on real images with manual annotations to demonstrate the impact of the synthesized data to our method.

From the 68 real BigNeuron images used in [S3], we selected 54 images to train the SPE-DNR. The

remaining 14 images were in the BigNeuron test dataset of this work. In total 209,259 training samples were randomly generated from the real training images based on the manual annotations. The comparison was conducted on the 34 BigNeuron test images used in this paper. The experimental results are shown in Fig. S3. For simplicity, we use ‘REAL’ to represent the SPE-DNR trained on the real training images and ‘SYN’ to represent the SPE-DNR trained on the synthetic training images. From Fig. S3, we can see that ‘SYN’ outperforms ‘REAL’ in all the metrics. The performance spread of ‘SYN’ is substantially smaller than ‘REAL’, indicating that the synthetic training images help to increase the robustness of the SPE-DNR. The experimental results demonstrate the advantage of using synthetic training images. Moreover, it can be seen that ‘REAL’ outperforms FMST, MOST, APP2 and TreMap in most of the metrics, and it is comparable to R2. This indicates that the SPE-DNR can also obtain competitive results using real training images with imperfect annotations, demonstrating its effectiveness.

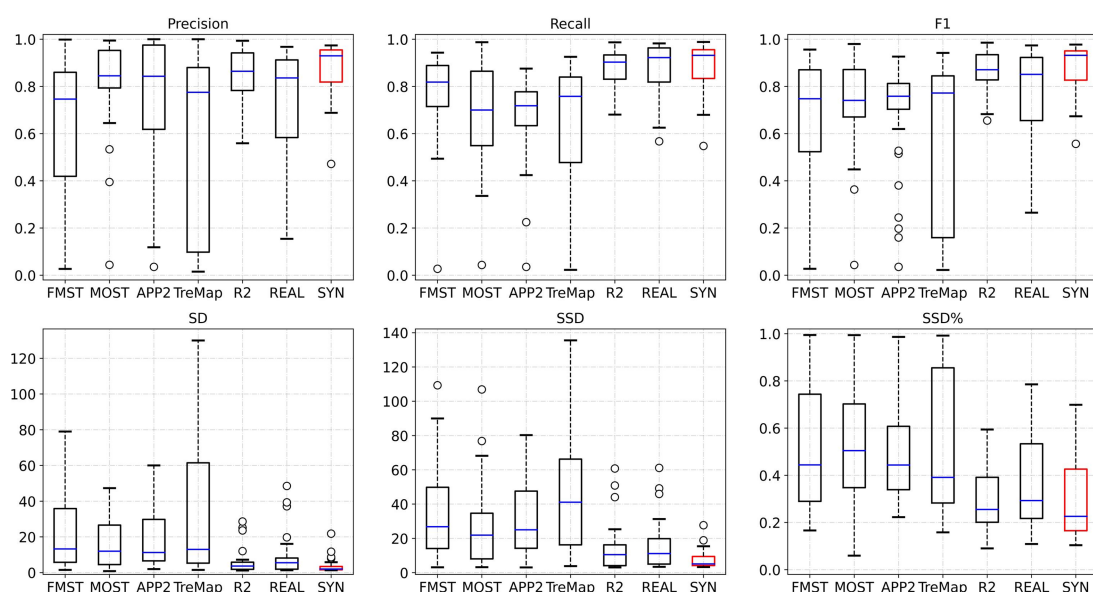


Fig. S3. Performance comparison for the BigNeuron dataset. ‘REAL’ represents the performance of the SPE-DNR trained on the real training images, whereas ‘SYN’ represents that on the synthetic training images.

References

- [S1] H. Jeelani, H. Liang, S. T. Acton, and D. S. Weller, “Content-aware enhancement of images with filamentous structures,” *IEEE Trans. Image Process.*, vol. 28, no. 7, pp. 3451–3461, Jul. 2019.
- [S2] W. Chen *et al.*, “Spherical-patches extraction for deep-learning based critical points detection in 3D neuron microscopy images,” *IEEE Trans. Med. Imag.*, vol. 40, no. 2, pp. 527–538, Feb. 2021.
- [S3] R. Li, T. Zeng, H. Peng, and S. Ji, “Deep learning segmentation of optical microscopy images improves 3-D neuron reconstruction,” *IEEE Trans. Med. Imag.*, vol. 36, no. 7, pp. 1533–1541, Jul. 2017.